Journal of the European Ceramic Society 44 (2024) 277–283

Contents lists available at ScienceDirect

Journal of the European Ceramic Society

journal homepage: www.elsevier.com/locate/jeurceramsoc

A $TiSnNbTaGa_2O_{12}$ high-entropy microwave dielectric ceramic with rutile structure and near-zero τ_f

Lei Xiao [a], Lianwen Deng [b], Yingxiang Li [a], Zhenjun Qing [a], Yecheng Xi [a], Jiahui Zhu [a], Sen Peng [a,b,*]

[a] Provincial Key Laboratory of Informational Service for Rural Area of Southwestern Hunan, Shaoyang University, Shaoyang 422000, China
[b] School of Physics and Electronics, Central South University, Changsha 410083, China

ARTICLE INFO

Keywords:
$TiSnNbTaGa_2O_{12}$ high-entropy ceramics
Microwave dielectric properties
P–V–L theory

ABSTRACT

$TiSnNbTaGa_2O_{12}$ (TSNTGO) high–entropy dielectric ceramic was successful synthesized using the solid-state reaction method. X–ray diffraction (XRD), Rietveld refinement and transmission electron microscopy (TEM) were used to verify that all samples have rutile structure of P42–mnm space group. The analysis of Raman spectra proved that the ε_r exhibited a contrary changing trend as that of Raman shift near 822 cm^{-1}, and the same similar relationship occurred between $Q\times f$ values and full width at half maximum (FWHM). The exploration of complex chemical bonding theory (P–V–L theory) for TSNTGO ceramics suggested that the bond ionicity played a dominant role in ε_r, while $Q\times f$ and τ_f were primarily determined by lattice energy and bond energy, respectively. Notably, the TSNTGO ceramics sintered at 1275 ℃ demonstrated optimal microwave dielectric properties of ε_r = 33.62 ± 0.03, $Q\times f$ = 51,832 ± 1000 GHz (f_0 = 6.4 GHz), and τ_f = –0.38 ± 0.16 ppm/℃.

1. Introduction

With the increasing number of mobile communication users, the microwave frequency band has become an important part of the mobile communication field, as it offers high transmission speed and large communication capacity [1–4]. Microwave communication technology was favored for its advantages of long communication distance, high communication quality, and not requiring specialized communication media [5–7]. Microwave dielectric ceramic is a type of functional material that must possess microwave dielectric properties in addition to certain physical properties [8–10]. Specifically, the dielectric constant (ε_r) should be large to enable device miniaturization, the quality factor ($Q\times f$) should be high to ensure outstanding frequency selectivity of the material, and the temperature coefficient of resonance frequency (τ_f) should be near zero to achieve high thermal stability, which are key factors in evaluating the performance of ceramic materials [11,12].

Notably, Ga-based ceramics have demonstrated excellent dielectric properties [13,14]. For instance, Chen et al. reported that $LiGaO_2$ ceramics sintered at 1240 ℃ possessed dielectric properties of ε_r = 5.82, $Q\times f$ = 24,500 GHz, and τ_f = –74.3 ppm/℃ [13]. Similarly, Ma et al. found that excellent dielectric properties (11.8 of ε_r, −32 ppm/℃ of τ_f, and 32,500 GHz of $Q\times f$) were achieved for $SrLaGa_3O_7$ ceramics sintered at 1425 ℃ [14]. However, due to their high τ_f value, the aforementioned Ga–based ceramics can not be used in practical applications. In recent years, high–entropy oxides (HEOs) [15] have been gradually applied in microwave dielectric ceramics, and their special structures with single-phase or solid-phase solutions were considered to optimize certain properties [16,17]. For case, Xiang et al. [18] reported that superior microwave dielectric performance of ε_r = 9.0, $Q\times f$ = 11,700 GHz (12.6 GHz), and τ_f = –7.4 ppm/℃ were acquired for Li$(Gd_{0.2}Ho_{0.2}Er_{0.2}Yb_{0.2}Lu_{0.2})GeO_4$ high–entropy ceramics. Similarly, Lin et al. [19] reported another high-entropy microwave dielectric ceramic $Sr(La_{0.2}Nd_{0.2}Sm_{0.2}Eu_{0.2}Gd_{0.2})AlO_4$ with ε_r = 18.6, $Q\times f$ = 14,509 GHz, τ_f = –6 ppm /°C. Related studies have demonstrated that a new technique for bringing the τ_f value near zero can be achieved by combining high–entropy compositional architecture with dielectric ceramics. Although the τ_f values of the Li$(Gd_{0.2}Ho_{0.2}Er_{0.2}Yb_{0.2}Lu_{0.2})GeO_4$ and Sr$(La_{0.2}Nd_{0.2}Sm_{0.2}Eu_{0.2}Gd_{0.2})AlO_4$ high–entropy ceramics were respectable, their possibilities for development were limited by their low $Q\times f$ values. The need to find a high–entropy ceramic with a superior $Q\times f$ value and a near-zero τ_f value arises as a result. It has been discovered that $TiSnNbTaGa_2O_{12}$ possesses a high $Q\times f$ value and a near-zero τ_f

* Corresponding author at: Provincial Key Laboratory of Informational Service for Rural Area of Southwestern Hunan, Shaoyang University, Shaoyang 422000, China.
E-mail address: psen126@hnsyu.edu.cn (S. Peng).

https://doi.org/10.1016/j.jeurceramsoc.2023.08.031
Received 18 May 2023; Received in revised form 14 August 2023; Accepted 19 August 2023
Available online 21 August 2023

value during the exploration of new high-entropy ceramics. The photoelectric performance of the high–entropy oxide $TiSnNbTaGa_2O_{12}$ (TSNTGO) has only been examined, however, its dielectric properties have not yet been researched [20]. Therefore, a series of $TiSnNbTaGa_2O_{12}$ ceramics were prepared, and the internal and external factors affecting dielectric properties were investigated in detail.

In this work, high–entropy microwave ceramic named $TiSnNbTaGa_2O_{12}$ was synthesized through conventional solid-state reaction method, aiming to examine its dielectric properties. The comprehensive analyses, including XRD, TEM, Rietveld refinement, Raman spectroscopy, and XPS were applied to investigate the crystal structure, microstructure, and dielectric properties of $TiSnNbTaGa_2O_{12}$ ceramics. Furthermore, this work utilized the P–V–L theory to explore the correlation between the chemical bonds and dielectric properties of TSNTGO ceramics comprehensively. The primary objective was to offer both theoretical and practical insight into optimizing the performance of dielectric ceramics through analyzing the dielectric characteristics of TSNTGO ceramic materials.

2. Experimental procedures

A high–entropy dielectric ceramic with the chemical formula $TiSnNbTaGa_2O_{12}$ was synthesized using the solid-state reaction method. The starting materials including TiO_2, SnO_2, Nb_2O_5, Ta_2O_5, and Ga_2O_3 (purity > 99.9%, Aladdin, China) were weighed according to their stoichiometric ratios. The raw materials were wet-milled for 12 h with zirconia balls and deionized water, followed by drying at 85 ℃ and calcining at 1300 ℃ for 6 h in a muffle furnace to obtain the pure TSNTGO phase. Next, for lowering the sintering temperature (S.T.), 3 wt % $MnCO_3$ was added into the ceramic samples for secondary ball-milling. The detailed process of secondary ball-milling was to ball-mill the calcined powders and 3 wt% $MnCO_3$ using alcohol and zirconia ball for 12 h, and then the mixtures were dried in a drying oven at 85 ℃ for 20 h. Following the production of the dried powders, an even distribution was achieved by blending it with 8 wt% polyvinyl alcohol (PVA). To prepare cylindrical pillars with 15 mm × 8 mm, the powders were compressed using hydraulic press and tabletting die. Lastly, the compacted pillars underwent a sintering process in a muffle furnace within a temperature range of 1250–1350 ℃ for 4 h.

The apparent density was obtained by the Archimedes principle. The composition of TSNTGO ceramics was determined and refined using X-ray diffraction (XRD, Micro 600, Japan) and GSAS software, respectively. The test parameters were set as follows: the scanning angle range (2θ) was 20–80 °, the step angle was 0.04, and the sampling time of each step was 6 s. Raman spectroscopy (Renishaw, UK, 532 nm) and X-ray photoelectron spectroscopy (XPS, VG Scientific, ESCALAB 250) were employed to examine the internal lattice vibrations and chemical valence states of TSNTGO ceramics, respectively. A scanning electron microscope (SEM, su1510, Hitachi, Japan) was utilized for inspecting the microstructure of thermal-etched TSNTGO ceramics. The cross-sections of the samples were polished and then thermally etched at a sintering temperature of 30 ℃ below the sintering temperature. Nano Measurer software was used to calculate the average grain size (AG). The ε_r and $Q\times f$ values were assessed using an Agilent E8363B network

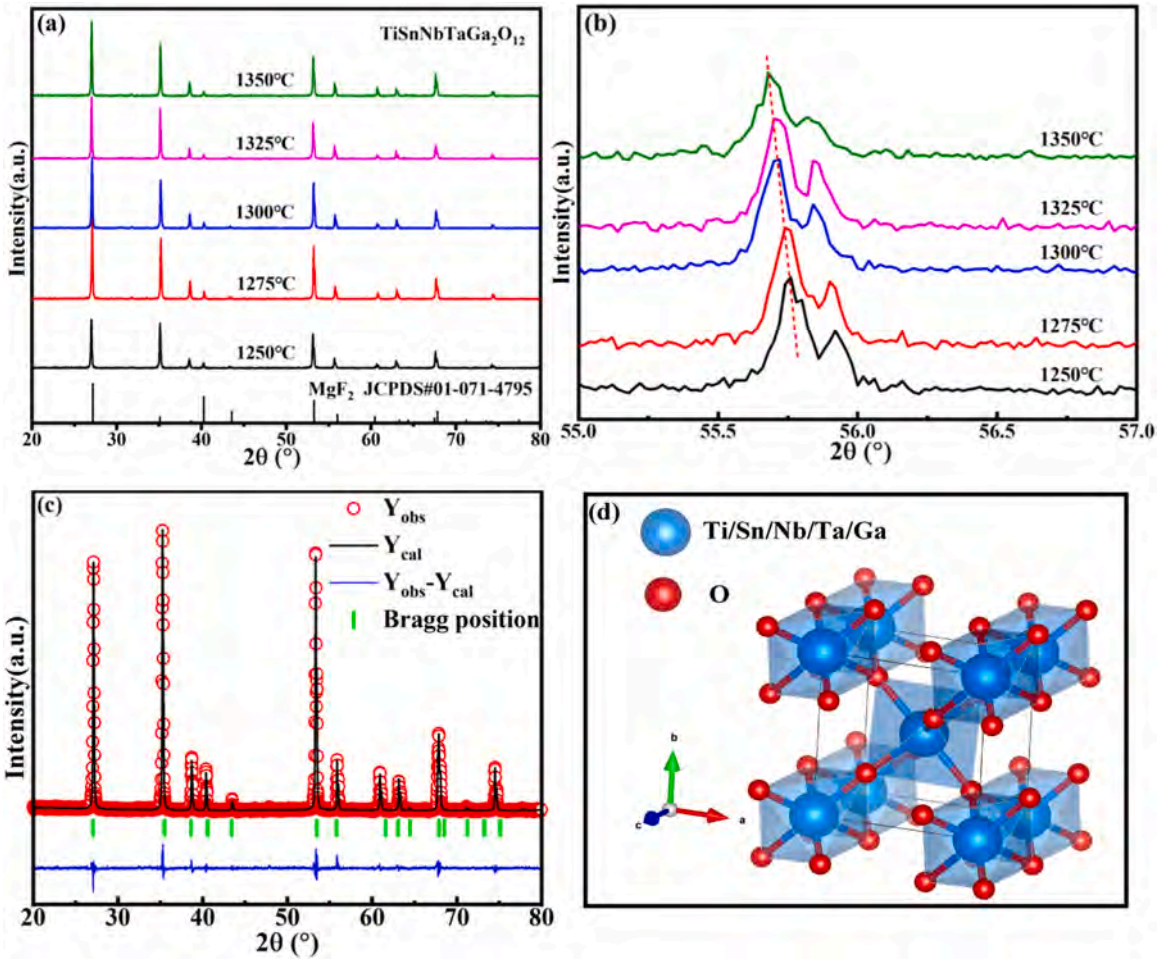

Fig. 1. (a) The XRD patterns of TSNTGO ceramics; (b) The amplified XRD patterns at 55–57°; (c) The Rietveld refinement patterns of TSNTGO ceramics sintered at 1275 ℃; (d) Structure diagram of TSNTGO ceramics.

analyzer. Ultimately, the τ_f value was ascertained through the given formula at resonance frequencies of 20 °C and 80 °C:

$$\tau_f = \frac{f_{80} - f_{20}}{f_{20} \times (80 - 20)} \times 10^6 (\text{ppm}/\text{℃}) \quad (1)$$

where f_{80} and f_{20} were the resonant frequency at 80 °C and 20 °C, respectively.

3. Results and discussion

The XRD patterns were recorded in Fig. 1(a), where all XRD diffraction peaks were compared with those of MgF_2 (PDF: 01–071–4795) to confirm the phase structure. The results indicated that all samples presented the pure phase and rutile structure with space group P42–mnm [20]. Fig. 1(b) demonstrated that the diffraction peak shifted towards a lower angle as increased sintering temperature. This phenomenon could be attributed to the expansion of the lattice, which led to an increase in cell volume [21]. Refined patterns of the TSNTGO ceramics sintered at 1275 ℃ and the corresponding lattice parameters at different sintering temperatures were illustrated in Fig. 1(c) and Table 1, respectively. As depicted in Fig. 1(c), the Rietveld refinement patterns of the sample sintered at 1275 ℃ exhibited excellent structural stability and a good fit for all diffraction peaks. The data acquired from Table 1 reflected that the R factors for all TSNTGO ceramics were below 10%, indicating a high level of precision in this finding. The crystal structure of MgF_2 was used as a model for the Rietveld refinement of TSNTGO ceramics [22], as depicted in Fig. 1(d). The oxygen octahedron was formed by the arrangement of O anions surrounding the Ti/Sn/Nb/-Ta/Ga cations in the center.

Fig. 2(a)–(b) depict the selected area electron diffraction (SAED) and high resolution transmission electron microscope (HRTEM) images of TSNTGO ceramics. Fig. 2(b) displays two interplanar spacings of 2.49 Å and 2.19 Å, corresponding to the $(10\bar{1})$ and $(11\bar{1})$ crystal planes of tetragonal rutile structure. The same atomic arrangement law as the crystal structure could be observed from the HRTEM map. The TEM results further proved the conclusion of XRD, and the TSNTGO ceramic obtained in this work was determined to be a tetragonal rutile structure with space group P42-mnm. Among them, the P42–mnm space group was similar to magnesium fluoride, consistent with the observational results [23]. Fig. 2(c) shows the relative density of TSNTGO ceramics after sintering at 1250–1350 ℃. At 1275 ℃, a maximum value of 97.72% was acquired for relative density, while a decline in relative density was observed between 1275 ℃ and 1350 ℃. Moreover, all samples exhibited a typical compactness with a relative density greater than 96.6%, and the relative density presented a strictly identical trend as that of $Q\times f$ value, establishing that densification played a positive role in influencing the dielectric properties.

Fig. S1 displays the SEM images of polished and thermal-etched TSNTGO ceramics and the corresponding average grain sizes. With an increase of sintering temperature, the grain size of TSNTGO ceramics grew from 1.04 μm to 1.68 μm. At 1275 °C, the samples demonstrated a favorable dense microstructure, and characterized by noticeably uniform grains, as shown in Fig. 2(d). The corresponding increase in relative density aligned with the changes observed in the $Q\times f$ value of the samples sintered at 1250–1275 ℃. At this time, both grain size and relative density played a positive role in determining the $Q\times f$ value. However, when the sintering temperature exceeded 1275 °C, the inhomogeneous grain growth distribution caused a decrease in density, resulting in a continuous decline in dielectric properties.

Table 1
The lattice parameters and refinement data of TSNTGO ceramics after refinement treatment.

S.T.	1250 ℃	1275 ℃	1300 ℃	1325 ℃	1350 ℃
a=b (Å)	4.65606	4.66041	4.66092	4.66093	4.66098
c (Å)	3.0446	3.045	3.04533	3.04533	3.04536
V_{cell} (Å^3)	66.003598	66.135638	66.157288	66.157572	66.159646
R_{wp} (%)	7.96	7.76	8.09	8.72	8.83
R_p (%)	6.74	6.58	6.82	7.09	7.14
χ^2	1.664	1.617	1.683	1.783	1.803

Fig. 3 displays the XPS spectrum obtained after sintering the TSNTGO ceramic at 1275 ℃, along with the results of peak division simulation for each metal element. All peaks had been calibrated using the C 1 s peak at 284.8 eV. As shown in Fig. 3(b), the absorption bands in the oxygen octahedron formed by Ti and six oxygen atoms were divided into two series of $2p_{3/2}$ and $2p_{1/2}$. The energy positions of Ti atom were consistent with that of Ti in titanium dioxide, indicating the existence of Ti^{4+} in TSNTGO ceramic [24]. Fig. 3(c) illustrates the spectrum of Sn in TSNTGO ceramic. The Sn 3d spectrum exhibited two peaks of $3d_{5/2}$ and $3d_{3/2}$ at 486.23 eV and 494.73 eV, respectively. This observation was consistent with the finding reported by K. Mašek et al. [25], which confirmed the existence of Sn^{4+} in a compound form in the sample. The spin orbital splitting of Nb atom occurred at binding energies of 209.83 eV and 207.03 eV [26], resulting in the formation of corresponding peaks of Nb $3d_{3/2}$ and Nb $3d_{5/2}$. Additionally, the XPS spectrum of Ta shows two weakly bound binding energy (BE) peaks, located in the Ta 4 $f_{5/2}$ series with a binding energy near 25.93 eV and the Ta 4 $f_{7/2}$ series with a binding energy near 19.73 eV, respectively [27,28]. These results confirmed the presence of Nb^{5+} and Ta^{5+} in TSNTGO ceramic. The fitted XPS spectrum depicted the distinct peaks associated with Ga $2p_{3/2}$ and Ga $2p_{1/2}$, exhibiting binding energies at 1117.83 eV and 1144.73 eV, correspondingly. The difference in their binding energies of 26.9 eV was consistent with the reference value, which was indexed to Ga^{3+} [29]. Therefore, the chemical valence states of cations such as Ti, Sn, Nb, Ta, and Ga in TSNTGO ceramics were determined to be +4, +4, +5, +5, and +3, respectively. XPS analysis showed that no abnormal valence elements existed in the TSNTGO ceramics affecting the structure and dielectric properties.

As illustrated in Fig. 4(a), The Raman spectra of TSNTGO ceramics exhibit the similar curve profiles, indicating that the samples exhibit structural stability at different temperatures. Fig. 4(b) presents the results of Gaussian fitting of the Raman spectra, which revealed the presence of seven Raman modes. Some peaks were not observed, possibly due to the weak intensity of certain Raman modes in the sample or the low instrument resolution [30]. The peak near 87 cm^{-1} was attributed to the shift of the oxygen octahedron [31], while the rotational mode of the cation was responsible for the peaks near 128 cm^{-1} [31]. The vibrational stretching of the Nb–O bond was observed around 263 cm^{-1} [32]. The internal motions of the GaO_4 tetrahedron accounted for the Raman peaks within the range of 300–600 cm^{-1} [33], whereas the vibrational peak in proximity to 663 cm^{-1} resulted from the tension-induced vibrational mode of the Ti–O bond in the TaO_6 octahedral structure [34]. The vibrational mode peak observed at approximately 822 cm^{-1} was related to the symmetric oscillation of the Ta–O bond in the TaO_6 octahedral structure [34]. Overall, the results of Raman analyses demonstrated the structural stability of the TSNTGO ceramics and provided valuable insights into the vibrational modes and structural properties of the materials.

Fig. 5 illustrates the dielectric properties of TSNTGO ceramics sintered at 1250–1350 ℃. Raman spectroscopy could be widely used to analyze the ε_r and $Q\times f$ [35,36]. There were some changes in the Raman peaks of TaO_6 oxygen octahedron near 822 cm^{-1} at different sintering temperatures. It was found that as the sintering temperature increased, the ε_r showed a contrary changing trend as that of Raman shift, and the same similar relationship occurred between $Q\times f$ values and FWHM, which was consistent with the report by Cai et al. [35]. Dielectric constant was correlated with the rigidity of the oxygen octahedron, which was the internal bond strength. It was reported that, the low-angular displacement of the Raman peak indicated that the oxygen octahedron decreased in rigidity, corresponding to the increase of dielectric constant [36]. As depicted in Fig. 5(a), the ε_r initially increased from 32.81 to

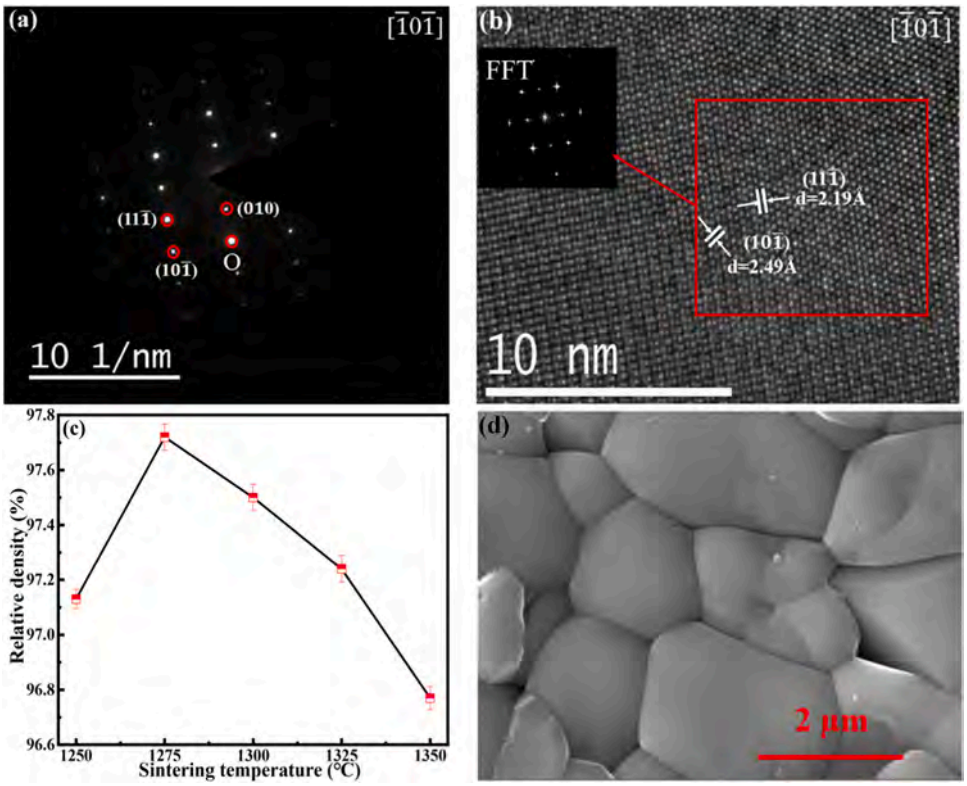

Fig. 2. (a) The SAED pattern of TSNTGO ceramics; (b) The HRTEM image of TSNTGO ceramics; (c) The relative density of TSNTGO ceramics; (d) SEM image of TSNTGO ceramics sintered at 1275 °C.

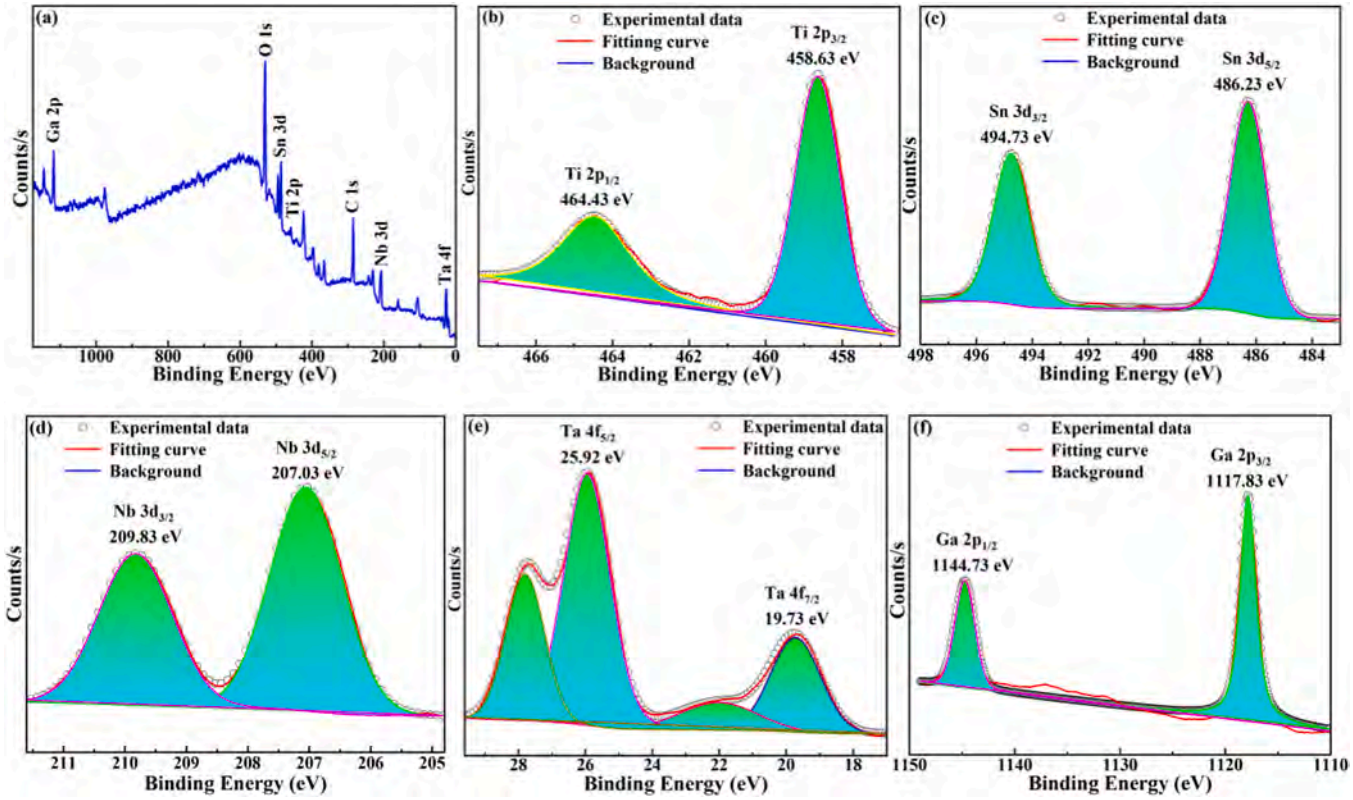

Fig. 3. XPS spectra of the TSNTGO ceramics sintered at 1275 ℃ with (a) full spectrum, (b) Ti 2p, (c) Sn 3d, (d) Nb 3d, (e) Ta 4 f, and (f) Ga 2p.

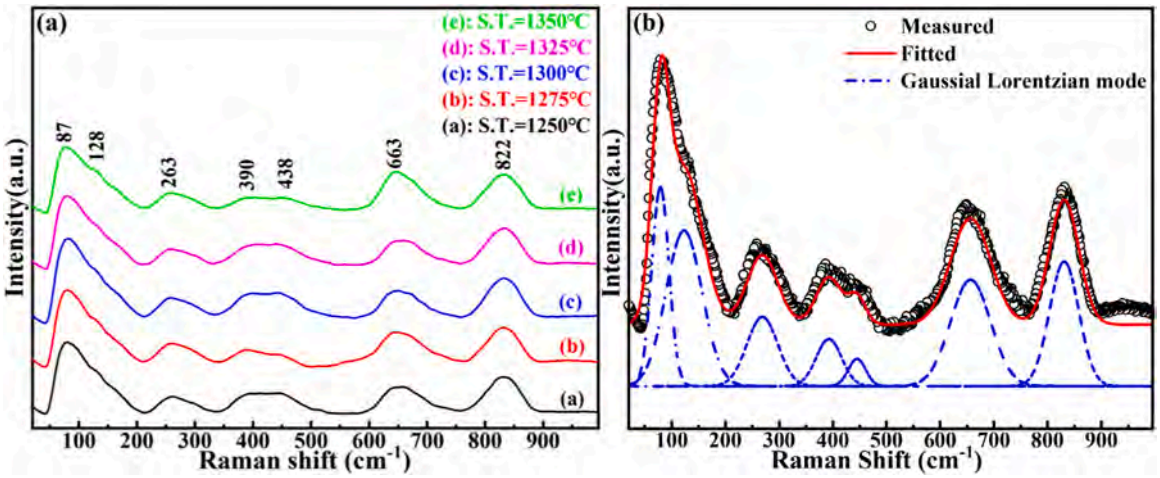

Fig. 4. (a) The Raman spectra of TSNTGO ceramics sintered at different temperatures; (b) the Gauss-Lorenzian deconvolution for TSNTGO ceramics sintered at 1275 ℃.

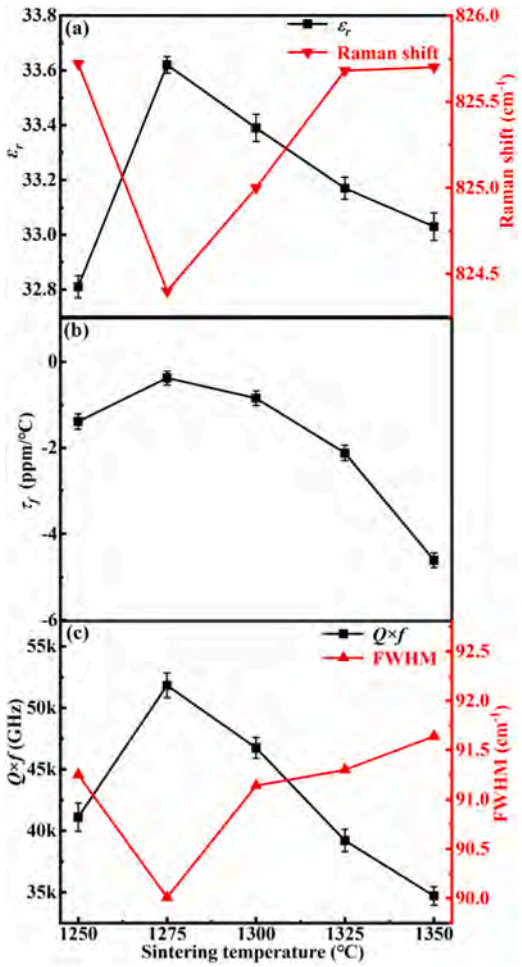

Fig. 5. (a) ε_r and Raman shift, (b) τ_f values, (c) $Q\times f$ values and FWHM of the TSNTGO ceramics as a function of the sintering temperatures.

33.62, and then decreased to 33.03, exhibiting an opposite changing trend as that of Raman shift. As depicted in Fig. 5(b), the τ_f value varied within the range of −0.38 to −4.61 ppm/℃, illustrating that the variation of temperature had no significant influences on the τ_f value of TSNTGO ceramics. Fig. 5(c) reveals that the $Q\times f$ value initially increased from 41,105 GHz to 51,832 GHz due to the combined effect of densification and FWHM, and then decreased with sintering temperature. SEM images revealed that the decrease in density was caused by excessive combustion, thereby damaging the $Q\times f$ value. Additionally, an increase in the FWHM was found to correspond to an increase in the damping coefficient, resulting in a decrease in $Q\times f$ value [35].

An examination of the connection between dielectric properties and the characteristics of chemical bonds in TSNTGO ceramics was conducted based on the chemical bond theory. Table S1 presents the lattice energy (U_b), bond energy (E_b), and thermal expansion coefficient (α_L) of TSNTGO ceramics sintered at the temperature range of 1250–1350 °C. Fig. 6 depicts the f_i, E_b, and U_b for various bonds in TSNTGO ceramics sintered at 1275 °C. All formulas and detailed calculation results obtained from P–V–L theory could be found in the Tables S1–S11.

The stability of the crystal structure was determined by the E_b and α_L [8]. Generally, a more stable crystal structure resulted in a higher E_b value, a lower α_L value, and a smaller the absolute value of τ_f. τ_f was closely related to both E_b and α_L for all samples. However, when the sintering temperature exceeded 1275 °C, the crystal structure became distorted and less stable, weakening the chemical bonds and causing the absolute value of τ_f to increase. From Tables S2–S11 and Fig. 6(a), the results revealed that the Nb-O bond contributed to 27.40% of the total E_b, playing a crucial role in regulating τ_f value.

U_b was general considered as a parameter, which was proportional to the $Q\times f$ value [8]. As demonstrated in Table S1, the U_b value of TSNTGO ceramics sintered at 1250–1350 °C displays a pattern of initially increasing followed by decreasing, which is consistent with the variation trend of $Q\times f$ value. According to the XRD and SEM analyses, it was found that all ceramic samples were pure phase and had high density. As a result, the $Q\times f$ value was predominantly affected by inherent losses. Typically, a more stable crystal structure led to a higher U_b, which in turn resulted in lower inherent and internal losses in sintered ceramics. As depicted in Fig. 6(b), a comparison of the contribution ratios of all bonds to the U_b value revealed that both the U_b of Ta–O and Nb–O bonds each accounted for the largest proportion of 22.83%. This finding indicated that Ta–O and Nb–O bonds played a crucial role in reducing internal loss and enhancing the $Q\times f$ value of TSNTGO ceramics. As illustrated in Fig. 6(c), comparison of the f_i values found that f_i(Ga–O) was the largest in all bond ionicity, indicating that the Ga–O bond had a great influence on the ε_r. The changing law of $Q\times f$ and τ_f obtained in this work were in good agreement with that of P–V–L theoretical calculation results, which once again proved the reliability of analyzing the dielectric properties of TSNTGO ceramics by chemical bonds.

The dielectric properties of Ga–based dielectric ceramics and high–entropy ceramics are presented in Table 2. Generally, it is crucial to possess a higher $Q\times f$ value for dielectric ceramics in practical

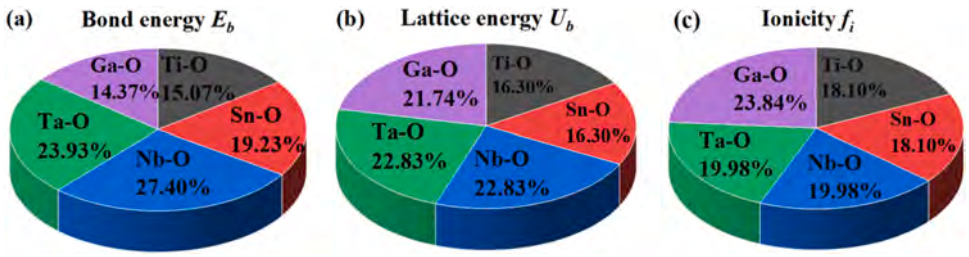

Fig. 6. Percentages of (a) E_b, (b) U_b, and (c) f_i of various bonds in TSNTGO ceramics.

Table 2
Performance comparison of some Ga-based dielectric ceramics and high–entropy ceramics.

Materials	S.T. (°C)	ε_r	$Q\times f$ (GHz)	τ_f (ppm/°C)	Ref.
$LiGaO_2$	1240	5.82	24,500	-74.3	[13]
$SrLaGa_3O_7$	1425	11.8	32,500	-32	[14]
$ZnGa_2O_4$	1400	9.8	83,000	-71	[37]
$LiMg_{0.5}Ti_{0.5}Ga_4O_8$	1260	11.28	85,360	-61.45	[38]
$Ba_2LaGa_{11}O_{20}$	1440	13.94	45,592	-16.3	[39]
$Li(Gd_{0.2}Ho_{0.2}Er_{0.2}Yb_{0.2}Lu_{0.2})GeO_4 + 3\%H_3BO_3$	900	9	11,700	-7.4	[18]
$Sr(La_{0.2}Nd_{0.2}Sm_{0.2}Eu_{0.2}Gd_{0.2})AlO_4$	1475	18.6	14,509	-6	[19]
$TiSnNbTaGa_2O_{12}$	1275	33.62	51,832	-0.38	This work

applications, also making sure that the τ_f value is near zero. Although $ZnGa_2O_4$ and $LiMg_{0.5}Ti_{0.5}Ga_4O_8$ ceramics possessed high $Q\times f$ value, their large τ_f values restricted their practical applications. The dielectric properties of $Li(Gd_{0.2}Ho_{0.2}Er_{0.2}Yb_{0.2}Lu_{0.2})GeO_4 + 3\%H_3BO_3$ and $Sr(La_{0.2}Nd_{0.2}Sm_{0.2}Eu_{0.2}Gd_{0.2})AlO_4$ ceramics reveal that high–entropy ceramics might be heralded as novel contender materials for microwave dielectric ceramics. It could be seen that other types of ceramics, as shown in Table 2, had some shortcomings in τ_f value, which need further improvement before they could be applied and produced. Conversely, TSNTGO ceramics exhibited desirable characteristics, including a high $Q\times f$ value and near-zero τ_f value, as well as a satisfying permittivity of 32 – 34. This demonstrated the potential of TSNTGO ceramics as candidate materials in communication applications.

4. Conclusions

A developed TSNTGO ceramic material with a near–zero τ_f value was produced using the solid–state reaction technique. The analyses of XRD, Rietveld refinement, and TEM confirmed that TSNTGO ceramics belonged to the rutile structure with a P42-mnm space group, and no secondary phase was detected in the samples. XPS analysis showed that the chemical valence states of Ti, Sn, Nb, Ta and Ga in TSNTGO ceramics were +4, +4, +5, +5 and +3, respectively, without any additional valence states. The results of SEM analysis demonstrated that TSNTGO ceramics possessed the highest density and homogeneous grain growth at 1275 °C. The increase in relative density contributed positively to the enhancement of the microwave dielectric properties for TSNTGO ceramics, achieving an optimal value of 97.72% at 1275 °C. Raman spectroscopy could be employed not only to investigate the crystal structure, but also to explore the dielectric properties of TSNTGO ceramics. The dielectric constant was found to be inversely proportional to Raman shift near 822 cm^{-1}. The $Q\times f$ value was primarily dependent on the FWHM, U_b, and densification of ceramic samples, and the τ_f value was closely related to the E_b and α_L values. Furthermore, the P–V–L theory analysis indicated that the Nb-O bond had a dominant role to regulate τ_f value, both Ta–O and Nb–O bonds played a crucial role in reducing internal loss and enhancing the $Q\times f$ value, and the Ga–O bond had a great influence on the ε_r of TSNTGO ceramics. Notably, the TSNTGO ceramics sintered at 1275 °C exhibited excellent performances of $\varepsilon_r = 33.62 \pm 0.03$, $Q\times f = 51{,}832 \pm 1000$ GHz ($f_0 = 6.4$ GHz), and $\tau_f = -0.38 \pm 0.16$ ppm/℃.

Declaration of Competing Interest

The authors declare that they have no known competing financial interests or personal relationships that could have appeared to influence the work reported in this paper.

Acknowledgments

This work was supported by the Natural Science Foundation of Hunan Province (Grant No. 2022JJ50197), and the Scientific Research Fund of Hunan Provincial Education Department (Grant No. 21B0681).

Appendix A. Supporting information

Supplementary data associated with this article can be found in the online version at doi:10.1016/j.jeurceramsoc.2023.08.031.

References

[1] X.J. Zhou, K.G. Wang, S. Hu, X.W. Luan, S. He, X. Wang, S.C. Zhou, X.L. Chen, H. F. Zhou, Preparation, structure and microwave dielectric properties of novel La_2MgGeO_6 ceramics with hexagonal structure and adjustment of its τ_f value, Ceram. Int. 47 (2021) 7783–7789, https://doi.org/10.1016/j.ceramint.2020.11.123.
[2] Z.J. Yang, Y. Tang, J. Li, W.S. Fang, J.Y. Ma, X.G. Zhao, L. Fang, Two low-εr phenakite-structure $LiAGeO_4$ (A = Al, Ga) microwave dielectric ceramics with different structure ordering, Ceram. Int. 47 (2021) 11022–11028, https://doi.org/10.1016/j.ceramint.2020.12.224.
[3] W.S. Fang, K. Cheng, H.C. Xiang, Y. Tang, Y.F. Zhai, C.X. Su, L. Fang, Phase composition and microwave dielectric properties of low permittivity $AGeO_3$ (A = Mg, Zn) ceramics, J. Alloy. Compd. 799 (2019) 495–500, https://doi.org/10.1016/j.jallcom.2019.05.312.
[4] Y. Tang, Z.W. Zhang, J. Li, M.Y. Xu, Y.F. Zhai, L. Duan, C.X. Sua, L.J. Liua, Y. H. Sunc, L. Fang, $A_3Y_2Ge_3O_{12}$ (A = Ca, Mg): Two novel microwave dielectric ceramics with contrasting τ_f and $Q \times f$, J. Eur. Ceram. Soc. 40 (2020) 3989–3995, https://doi.org/10.1016/j.jeurceramsoc.2020.04.052.
[5] S.M. Zhai, P. Liu, S.H. Wu, Novel ultra-low loss and low-fired $Li_8Mg_xTi_3O_{9+x}F_2$ microwave dielectric ceramics for resonator antenna applications, J. Eur. Ceram. Soci. 43 (2023) 3331–3337, https://doi.org/10.1016/j.jeurceramsoc.2023.01.041.
[6] X.W. Hu, J.W. Chen, J. Li, H.C. Xiang, Y. Tang, L. Fang, Contrasting microwave dielectric properties of zircon-structured $AEuV_2O_8$ (A = Bi, La) ceramics, J. Eur. Ceram. Soc. 42 (2022) 7461–7467, https://doi.org/10.1016/j.jeurceramsoc.2022.09.007.
[7] Z. Xing, J.H. Weng, C. Ma, Optimization of Zn_2GeO_4 microwave dielectric ceramics via Cu substitution and B_2O_3 sintering aid for LTCC application, Mater. Today Commun. 34 (2023) 105354–105361, https://doi.org/10.1016/j.mtcomm.2023.105354.
[8] M.F. Zhou, C.C. Hu, J.B. Yin, Y. Jiang, B. Liu, K.X. Song, Cold sintering optimized SrF_2 microwave dielectric ceramics for the development of dielectric resonator antenna at 5G millimeter-wave band, Ceram. Int. 48 (2022) 29847–29853, https://doi.org/10.1016/j.ceramint.2022.06.249.
[9] A. Zhang, H.Q. Fan, D.W. Hou, F. Yang, Y.Q. Chen, W.J. Wang, W.Q. Dong, Structure refinement, defects evolution and calcium doping of Sr_2CeO_4 microwave dielectric ceramics with high quality factor, Ceram. Int. 48 (2022) 26217–26225, https://doi.org/10.1016/j.ceramint.2022.05.303.

[10] Y.Q. Jia, W.B. Hong, L. Li, S.Y. Wu, B. Liu, X.M. Chen, Dense LiF microwave dielectric ceramics with near-zero linear shrinkage during sintering, Ceram. Int. 48 (2022) 28463–28470, https://doi.org/10.1016/j.ceramint.2022.06.160.
[11] Z.H. Wang, J.Q. Chen, H.C. Xiang, L. Fang, Structural and chemical bond characteristics of microwave dielectric ceramics $Sm_{3-x}Bi_xGa_5O_{12}$, Ceram. Int. 48 (2022) 18723–18729, https://doi.org/10.1016/j.ceramint.2022.03.146.
[12] X.Q. Chen, H. Li, P.C. Zhang, H.L. Hu, G.T. Chen, G.S. Li, A low-permittivity microwave dielectric ceramic $BaZnP_2O_7$ and its performance modification, J. Am. Ceram. Soc. 104 (2021) 5214–5223, https://doi.org/10.1111/jace.17839.
[13] J.Q. Chen, W.S. Fang, L.Y. Ao, Y. Tang, J. Li, L.J. Liu, L. Fang, Structure and chemical bond characteristics of two low-εr microwave dielectric ceramics $LiBO_2$ (B = Ga, In) with opposite τ_f, J. Eur. Ceram. Soc. 41 (2021) 3452–3458, https://doi.org/10.1016/j.jeurceramsoc.2021.01.024.
[14] J.Y. Ma, J.Q. Chen, H.C. Xiang, J. Li, Y. Tang, L. Fang, Modulation of microwave dielectric properties in melilite-structured $SrREGa_3O_7$ (RE = La, Pr) ceramics, Ceram. Int. 48 (2022) 6218–6224, https://doi.org/10.1016/j.ceramint.2021.11.162.
[15] D. Bérardan, S. Franger, D. Dragoe, Colossal dielectric constant in high entropy oxides, Phys. Status Solidi RRL 10 (2016) 328–333, https://doi.org/10.1002/pssr.201600043.
[16] K. Liu, H.W. Zhang, C. Liu, J. Li, L. Shi, X.Y. Wang, D.N. Zhang, Crystal structure and microwave dielectric properties of $(Mg_{0.2}Ni_{0.2}Zn_{0.2}Co_{0.2}Mn_{0.2})_2SiO_4$-a novel high-entropy ceramic, Ceram. Int. 48 (2022) 23307–23313, https://doi.org/10.1016/j.ceramint.2022.04.317.
[17] B. Cantor, I. Chang, P. Knight, A.J.B. Vincent, Microstructural development in equiatomic multicomponent alloys, Mater. Sci. Eng. A Struct. 375–377 (2004) 213–218, https://doi.org/10.1016/j.msea.2003.10.257.
[18] H.C. Xiang, L. Yao, J.Q. Chen, A.H. Yang, H.T. Yang, L. Fang, Microwave dielectric high-entropy ceramic $Li(Gd_{0.2}Ho_{0.2}Er_{0.2}Yb_{0.2}Lu_{0.2})GeO_4$ with stable temperature coefficient for low-temperature cofired ceramic technologies, J. Mater. Sci. Technol. 93 (2021) 28–32, https://doi.org/10.1016/j.jmst.2021.03.057.
[19] F.L. Lin, B. Liu, C.C. Hu, K.X. Song, Novel high-entropy microwave dielectric ceramics $Sr(La_{0.2}Nd_{0.2}Sm_{0.2}Eu_{0.2}Gd_{0.2})AlO_4$ with excellent temperature stability and mechanical properties, J. Eur. Ceram. Soc. 43 (2023) 2506–2512, https://doi.org/10.1016/j.jeurceramsoc.2023.01.028.
[20] Y. Yu, S. Liu, H. Wang, S. Zhang, N. Wang, W. Jiang, C. Liu, W. Ding, Z. Zhang, C. Dong, Synthesis and optoelectrical properties of $Ti_8Sn_8Nb_8Ta_8Me_{16}O_{96}$ (Me=Ga, Fe) rutile structure high entropy oxides, Vacuum 203 (2022) 111315–111320, https://doi.org/10.1016/j.vacuum.2022.111315.
[21] J. Bao, W.J. Guo, H. Kimura, Y.P. Zhang, J.L. Du, Y.Y. Zhou, Y. Ma, H.T. Wu, Z. X. Yue, Crystal structures, bond characteristics, and dielectric properties of novel middle-ε_r Ln3NbO7 (Ln = Nd, Sm) microwave dielectric ceramics with opposite temperature coefficients, Ceram. Int. 48 (2022) 36900–36907, https://doi.org/10.1016/j.ceramint.2022.08.256.
[22] B. Liu, K. Sha, M. Zhou, K. Song, C. Hu, C. Lu, Cold sintering assisted CaF_2 microwave dielectric ceramics for C-band antenna applications, J. Eur. Ceram. 42 (2022) 5698–5704, https://doi.org/10.1016/j.jeurceramsoc.2022.06.018.
[23] S. Zhai, P. Liu, S. Zhang, A novel high-Q oxyfluoride $Li_4Mg_2NbO_6F$ microwave dielectric ceramic with low sintering temperature, J. Eur. Ceram. 41 (2021) 4478–4483, https://doi.org/10.1016/j.jeurceramsoc.2021.02.049.
[24] N.A. Zhuk, S.V. Nekipelov, V.N. Sivkov, N.A. Sekushin, V.P. Lutoev, B.A. Makeev, A.V. Koroleva, A.V. Fedorova, L.A. Koksharova, M.M. Ignatova, R.I. Korolev, Magnetic and electric properties, ESR, XPS and NEXAFS spectroscopy of $CaCu_3Ti_4O_{12}$ ceramics, Ceram. Int. 46 (2020) 21410–21420, https://doi.org/10.1016/j.ceramint.2020.05.239.
[25] K. Mašek, M. Václavu, P. Bábor, V. MatolÍn, Sn–CeO_2 thin films prepared by rf magnetron sputtering: XPS and SIMS study, Appl. Surf. Sci. 255 (2009) 6656–6660, https://doi.org/10.1016/j.apsusc.2009.02.080.
[26] L.X. Li, Y.T. Li, J.L. Qiao, M.K. Du, Developing high-$Q \times f$ value $MgNb_{2-x}Ta_xO_6$($0 \leq x \leq 0.8$) columbite ceramics and clarifying the impact mechanism of dielectric loss: crystal structure, Raman vibrations, microstructure, lattice defects, chemical bond characteristics, structural parameters, and microwave dielectric properties in-depth studies, J. Mater. Sci. Technol. 146 (2023) 186–199, https://doi.org/10.1016/j.jmst.2022.10.061.
[27] T. Jiang, H.W. Chen, L.B. Gao, Y.C. Hui, B.W. Deng, Z. Fang, J. Zhou, J.H. Zhang, The $Ba(Mg_{1/3}Ta_{2/3})O_3$ ceramic based X-band filter, Mater. Sci. Eng. B Adv. 280 (2022) 115681–115687, https://doi.org/10.1016/j.mseb.2022.115681.
[28] B. Helena, M. Lubomir, K. Alexandra, F. Martin, M. Erika, D. Juraj, S. Martin, K. Maria, S. Jiri, Structural and mechanical properties of $La_{1/3}NbO_3$ and $La_{1/3}TaO_3$ thin films prepared by chemical solution deposition☆, J. Rare Earths 35 (2017) 1115–1125, https://doi.org/10.1016/j.jre.2017.05.009.
[29] S.P. Wu, J.J. Xue, R. Wang, J.H. Li, Synthesis, characterization and microwave dielectric properties of spinel $MgGa_2O_4$ ceramic materials, J. Alloy. Compd. 585 (2014) 542–548, https://doi.org/10.1016/j.jallcom.2013.09.176.
[30] C.Z. Yin, K. Du, M. Zhang, J.Q. Yang, F. Wang, Y.B. Guo, M.F. Cheng, Y.Y. Cai, X. Q. Song, J. Khaliq, C.C. Li, W. Lei, W.Z. Lu, Novel low-ε_r and lightweight $LiBO_2$ microwave dielectric ceramics with good chemical compatibility with silver, J. Eur. Ceram. Soc. 42 (2022) 4580–4586, https://doi.org/10.1016/j.jeurceramsoc.2022.04.032.
[31] C.W.A. Paschoal, R.L. Moreira, C. Fantini, M.A. Pimenta, K.P. Surendran, M. T. Sebastian, Raman scattering study of $RETiTaO_6$ dielectric ceramics, J. Eur. Ceram. Soc. 23 (2003) 2661–2666, https://doi.org/10.1016/S0955-2219(03)00141-9.
[32] A.V. Kumar, V. Subramanian, V. Sivasubramanian, Enhanced microwave dielectric properties of $ZnNb_2O_6$ by heterovalent ion substitution, J. Alloy. Compd. 944 (2023) 169202–169209, https://doi.org/10.1016/j.jallcom.2023.169202.
[33] J.Y. Ma, J.Q. Chen, Y. Tang, J. Li, W.S. Fang, Y.M. Dai, L. Fang, Chemical bond and microwave dielectric properties of two novel low-ε_r AGa_4O_7 (A = Ca, Sr) ceramics, J. Eur. Ceram. Soc. 42 (2022) 478–484, https://doi.org/10.1016/j.jeurceramsoc.2021.10.005.
[34] L.T. Liu, W.J. Guo, S.J. Yan, P. Liu, J.L. Du, Y.P. Zhang, H.T. Wu, Y.G. Chen, Z. X. Yue, Microstructure, Raman spectroscopy, THz time domain spectrum and microwave dielectric properties of $Li_2Ti_{1-x}(Zn_{1/3}Ta_{2/3})_xO_3$ ceramics, Ceram. Int. 49 (2023) 6864–6872, https://doi.org/10.1016/j.ceramint.2022.10.169.
[35] C.Y. Cai, X.Q. Chen, H. Li, J. Xiao, C.W. Zhong, S.R. Zhang, Microwave dielectric properties of $Ca_{1-x}Sr_xMgSi_2O_6$ ceramics, Ceram. Int. 46 (2020) 27679–27685, https://doi.org/10.1016/j.ceramint.2020.07.265.
[36] J. Li, L. Fang, G. Zhao, C. Xing, H. Qiao, H. Chen, Z. Qi, Q. Wang, F. Shi, Correlation between vibrational modes, crystal structures, and dielectric properties of (1-x)$Ba(Mg_{1/3}Ta_{2/3})O_3$-$xBa(Co_{1/3}Nb_{2/3})O_3$ ceramics, J. Mater. Res. 33 (2018) 4071–4079, https://doi.org/10.1557/jmr.2018.272.
[37] X.C. Lu, B. Quan, K.L. Zheng, P. Chu, J. Wang, G.X. Shen, Q.T. Zhang, F. Xu, Sc modification induced short-range cation ordering and high microwave dielectric performance in $ZnGa_2O_4$ spinel ceramics, J. Alloy. Compd. 873 (2021) 159758–159764, https://doi.org/10.1016/j.jallcom.2021.159758.
[38] X.G. Zhao, Y. Tang, J. Li, W.S. Fang, L.Y. Ao, S.Y. Shen, L. Fang, The structure evolution and lattice energy of spinel-structured $Li(Mg_{0.5}Ti_{0.5})_xGa_{5-x}O_8$ microwave dielectric ceramics, Ceram. Int. 47 (2021) 31732–31739, https://doi.org/10.1016/j.ceramint.2021.08.053.
[39] L.Y. Ao, J. Li, Y. Tang, W.S. Fang, L.J. Liu, Y.H. Sun, L. Fang, Structure, far-infrared reflectance spectra, and microwave dielectric properties of $Ba_2MGa_{11}O_{20}$ (M = Bi, La) ceramics, Ceram. Int. 47 (2021) 11899–11905, https://doi.org/10.1016/j.ceramint.2021.01.030.